Exploring the use of numerical relativity waveforms in burst analysis of precessing black hole mergers

Sebastian Fischetti, James Healy, Laura Cadonati, Lionel London, Satyanarayan R. P. Mohapatra, and Deirdre Shoemaker

Exploring the Use of Numerical Relativity Waveforms in Burst Analysis of Precessing Black Hole Mergers

Sebastian Fischetti[1], James Healy[2], Laura Cadonati[1], Lionel
London[2], Satyanarayan R.P. Mohapatra[1], and Deirdre Shoemaker[2]

[1]*Department of Physics, University of Massachusetts, Amherst MA 01003-9337 and*
[2]*Center for Relativistic Astrophysics, 837 State Street, GeorgiaTech, Atlanta, GA 30332-0430*

Recent years have witnessed tremendous progress in numerical relativity and an ever improving performance of ground-based interferometric gravitational wave detectors. In preparation for Advanced LIGO and a new era in gravitational wave astronomy, the numerical relativity and gravitational wave data analysis communities are collaborating to ascertain the most useful role for numerical relativity waveforms in the detection and characterization of binary black hole coalescences. In this paper, we explore the detectability of equal mass, merging black hole binaries with precessing spins and total mass $M_T \in [80, 350]M_\odot$, using numerical relativity waveforms and template-less search algorithms designed for gravitational wave bursts. In particular, we present a systematic study using waveforms produced by the MAYAKRANC code that are added to colored, Gaussian noise and analyzed with the Omega burst search algorithm. Detection efficiency is weighed against the orientation of one of the black-hole's spin axes. We find a strong correlation between the detection efficiency and the radiated energy and angular momentum, and that the inclusion of the $\ell = 2$, $m = \pm 1, 0$ modes, at a minimum, is necessary to account for the full dynamics of precessing systems.

I. INTRODUCTION

The detection of gravitational waves is one of the most exciting developments expected for the next decade in Physics and Astronomy. Ground-based detectors, such as LIGO [1] and Virgo [2], have achieved their initial design sensitivity and are making progress toward their advanced configuration [3, 4]. According to stellar population synthesis models [5], Advanced LIGO and Advanced Virgo will be sensitive to measurable rates of compact binary coalescences, and open a new field of gravitational-wave astronomy.

There are many uncertainties in the amount and form of gravitational wave signals that will be first detected. We refer to gravitational wave bursts as transient signatures lasting between a few milliseconds and seconds in the detector sensitive band, as could be produced by core-collapse supernovae or the late stages of the merger of two intermediate-mass black holes, as well as serendipitous sources. Burst signatures are typically searched for with template-less algorithms that identify coincident excess power in multiple detectors [6, 7]. In particular, this paper focuses on the detectability of the mergers of compact objects with total mass $M_T \in [80, 350]M_\odot$, whose solutions require simulations of the non-linear Einstein field equations of General Relativity. The field of numerical relativity (NR) has produced solutions to the merger of two black holes [8–29] that are now being used as signals to test the performance of analysis routines [30] and to calibrate the analytical and phenomenological waveform families used as template banks in searches [31–33].

For systems with total mass greater than $\sim 80M_\odot$, the final stages of a binary black hole (BBH) coalescence, merger and ringdown, yield most signal-to-noise ratio (SNR) in ground-based detectors. This is the motivation for the work presented in this paper: a systematic study of how the parameters of the coalescence affect the detectability of mergers of BBHs in a burst search. We test the detectability of mergers in simulated Gaussian noise at the initial LIGO design sensitivity with the Omega algorithm [34], used by the LIGO-Virgo collaboration to search for gravitational wave bursts, with a fixed, single-detector threshold of SNR ≥ 5.5, chosen to match the definition of single-detector "trigger" in compact binary coalescence searches in real LIGO noise [35]. We are interested in the effects of both numerical and physical parameters; in this study, we focus on the effect of spin and its orientation as well as the number of included harmonics and gravitational-wave cycles.

This paper is organized as follows. In Section II, we explain how the waveforms are generated and how the Omega pipeline burst search algorithm works. In Section III, we explain how we use the NR waveforms to generate the simulated signals, and discuss the analysis and postprocessing of the data. Results are presented in Section IV, and conclusions in Section V.
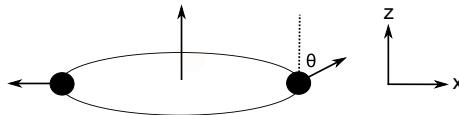
FIG. 1: Spin configuration used in the simulations for this work. The masses and spin magnitudes of the black holes are equal, and the orbit is initially quasi-circular.

II. BACKGROUND

A. NR Waveforms

The waveforms used in this work were generated using the vacuum BBH numerical relativity code MAYAKRANC, also used in previous studies [21, 36–38]. MAYAKRANC adopts the Baumgarte-Shapiro-Shibata-Nakamara formulation with moving puncture gauge conditions [9, 10] and the KRANC code generator [39]. Bowen-York extrinsic curvature is used to solve the momentum constraint initially [40], and the Hamiltonian constraint is solved using the TWOPUNCTURES spectral solver [41]. This study uses simulations of equal-mass black holes initially located on the x-axis, with momentum determined by the 3rd-order post-Newtonian angular momentum [42, 43], according to the geometry in Figure 1. Most simulations have an initial separation of $d/M = 6.2$, although two sets of simulations with larger initial separations of $d/M = 8$ and $d/M = 10$ are also included. Our code units are given by $M = m_1 + m_2 = 2m$, where m is the horizon mass of the initial black holes. In all simulations, the black holes are spinning, with $S_- = \{-a, 0, 0\}m$ and $S_+ = \{a\sin\theta, 0, a\cos\theta\}m$. We vary θ from $0°$ to $360°$ for a given a/m, and we consider three spin values: $a/m = \{0.2, 0.4, 0.6\}$. We hold d/M, a/m and the total initial mass of the back holes constant as we vary θ.

The grid structure for each run consists of ten levels of refinement provided by CARPET [44], a mesh refinement package for CACTUS [45]. We use sixth-order spatial finite differencing; the outer boundaries are located at $317M$, the finest resolution is $M/77$ and the waveforms are extracted at $75M$. A few waveforms have been generated at resolutions of $\{M/64, M/77, M/90\}$, with convergence consistent with our sixth-order code. The short (long) runs exhibit a phase error on the order of 5×10^{-3} (5×10^{-2}) radians and an amplitude error of $\approx 2\%$ ($\approx 5\%$). Similar accuracy can be expected in all runs we performed.

To characterize the NR runs, in Figure 2 we plot as a function of θ the ratio $E^{\rm rad}/M^{\rm ADM}$, that is the total radiated energy ($E^{\rm rad}$) normalized by the total mass of the system given by the Arnowitt-Deser-Misner mass ($M^{\rm ADM}$). The radiated energy varies from approximately 2.8% to almost 4.4 % of the total ADM mass. The minimum occurs when $\theta \approx 180°$ due to the way the system is configured initially. By keeping the initial separation fixed, the misalignment of the spin with the orbital angular momentum results in $\theta = 180°$ being the shortest run with very little inspiral before merger. The dashed line was computed using only the dominant mode, $\ell = 2$, $m = \pm 2$, the solid has all modes up to and including $\ell = 6$ and the dashed all the m-modes of $\ell = 2$ ($m = 0$, $m = \pm 1$, $m = \pm 2$). Not including all the $\ell = 2$ modes in computing $E^{\rm rad}$ clearly underestimates the energy radiated for some values of θ. Modes other than $\ell = 2$, however, contribute little to the total radiated energy, comparing solid and dashed.

In Figure 3, the solid curve is the total magnitude of the radiated angular momentum $J^{\rm rad}$, normalized by the initial angular momentum $J^{\rm init}$, while the dashed curve is the radiated angular momentum in the z direction $J_z^{\rm rad}$, normalized by $J_z^{\rm init}$ (the initial angular momentum was not fixed for all simulation runs). When the two curves align, the simulations are dominated by radiation in the z direction. As we approach $\theta = 250°$, the other components of the angular momentum contribute significantly. The importance of the numeric value of θ is only in its labeling of the binary dynamics, for example that $J_x^{\rm rad}$ is at a maximum for $\theta = 250°$.

B. Burst Searches

Unmodeled burst searches look for gravitational wave transients in LIGO and Virgo data without assumption on the waveform morphology [6, 7]. This is accomplished by searching for statistically significant excess signal energy in the strain time series. The advantage of this type of analysis is that, because it does not require knowledge of the waveform *a priori*, it has the potential to detect signals missed by other searches. The particular burst algorithm used for this study is the *Omega pipeline* [34]. This algorithm first whitens the data, then decomposes it into a bank of windowed complex exponentials characterized by a central time τ, frequency ϕ, and quality factor Q. The signal is tiled in the τ-ϕ-Q space, and any tiles with a normalized energy above some threshold are recorded as possible events. This search is equivalent to a matched filtering against whitened data using a template bank of sine-Gaussians.
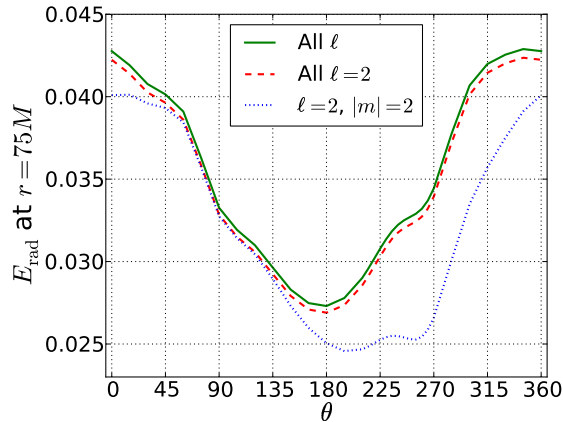
FIG. 2: Radiated energy, normalized by M^{ADM}, plotted versus θ for the series with $d/M = 6.2$ and $a/m = 0.6$. The radiated energy is computed at an extraction radius of $r = 75M$. The solid line is all $\ell \leq 6$, dashed: $\ell = 2$, dotted: dominant $\ell = 2$, $|m| = 2$.
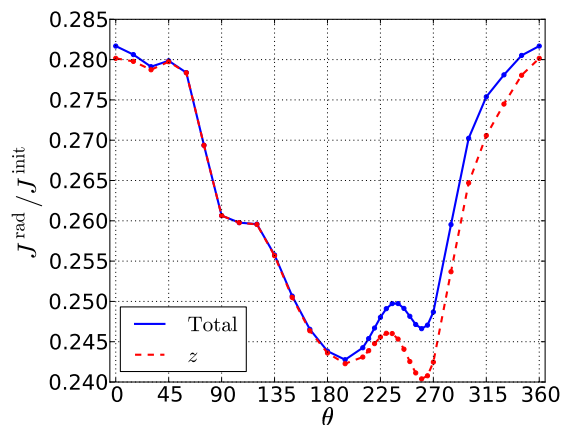

FIG. 3: The solid curve is the total magnitude of the radiated angular momentum normalized by the initial angular momentum for each run in the series with $d/M = 6.2$ and $a/m = 0.6$. The dashed curve is the radiated angular momentum in only the z direction with the same normalization.

III. METHODS

The NR waveforms were exchanged according to the data format described in [46]; the transformation between Ψ_4 and strain was done with the method outlined in [47]. In our study, NR waveforms are used to simulate signals from sources with random sky location and source inclination; the same set of simulation is scaled so as to effectively produce signals from 27 concentric shells at different radial distances from the detector. These simulated waveform are then injected into Gaussian noise colored to mimic the sensitivity of the initial LIGO design, shown in Figure 4. The combined signal and noise are then fed into Omega as a simulated detector output; the results are postprocessed to obtain the detection reach statistic described below.

Since this study is meant to provide a relatively broad insight into how efficiently burst searches detect BBH coalescences, we allowed some simplifications. First, we initially used only the dominant quadrupole modes of the waveforms, $(\ell, m) = (2, \pm 2)$, and disregarded all others. We found this has a noticeable impact on the waveform detectability; we discuss later the effect of using all $\ell = 2$ modes. Second, to disentangle waveform effects from that of non-stationary noise in real interferometer data, we didn't reproduce a full coherent multi-detector analysis at fixed false alarm rate, but instead only analyzed data from a single, ideal detector, chosen to be one of the LIGO 4km detectors, with a fixed SNR detection threshold.

This study is restricted to equal-mass systems with a total mass in the $80 - 350 \ M_\odot$ range. Because the frequency evolution of the waveforms scales as the total mass of the system, this range is chosen so that, in the initial detectors,
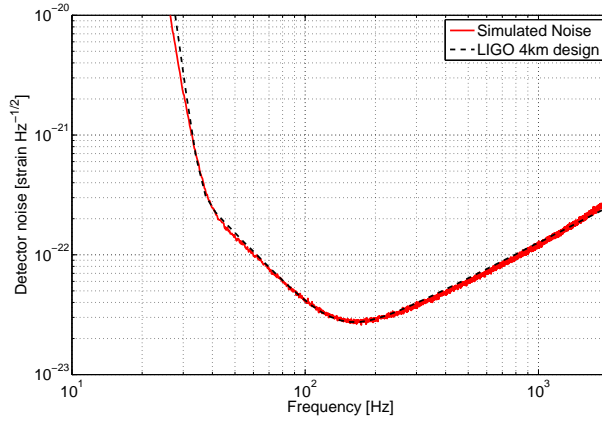
FIG. 4: The dashed line indicates the design sensitivity of LIGO's 4km detectors [1]; the continuous line is the spectrum of simulated noise used in our study.
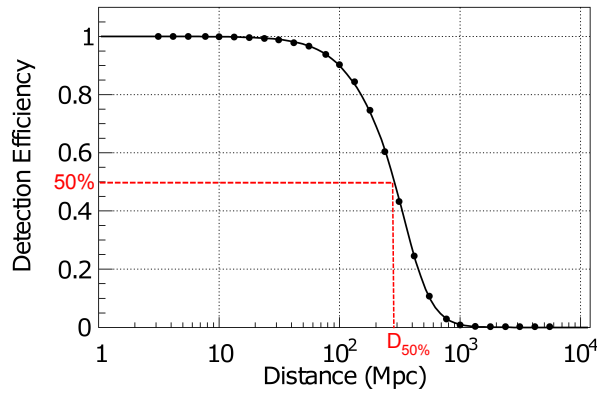

FIG. 5: A sample plot of detection efficiency as a function of distance to the source. Each point corresponds to the average detection efficiency of a spherical shell of radius equal to the distance in abscissa. The curve is a sigmoidal fit to the data, used to interpolate the distance $D_{50\%}$ at which the detection efficiency falls to 50%, referred to as the *reach* of the search. A binomial uncertainty is associated to each point, as described in the text, though the error bars are too small to be visible in this plot.

most of the SNR comes from the merger and ringdown portions of the waveform. For systems with lower total mass, there are enough inspiral cycles in the sensitive band to make it appropriate to use matched filtering techniques, as opposed to burst search algorithms [30]. For larger values of the total mass, the ringdown frequency falls below the 40 Hz high-pass filter applied to the data, and the waveform falls below the LIGO seismic noise barrier. Our best sensitivity is for systems with total mass in the $150 - 200$ $M_\odot$ range.

Once the Omega algorithms identifies instances of excess power in the simulated data, we compare the trigger list to the list of injected signals to identify which were missed or found. We use an SNR threshold of 5.5, chosen to match the definition of single-detector "trigger" in compact binary coalescence searches in real LIGO noise [35]. This threshold choice is one of convenience, for a study of the dependence of detectability on various other simulation parameters. In actual LIGO searches, the detection threshold will be determined by the rate of non-Gaussian noise transients and what is considered to be an acceptable false alarm probability [6, 7]. For each concentric shell in our simulated sky, we compute an average detection efficiency ε, defined as the ratio of the number of found signals to the total number of injected signals in that shell. The uncertainty in the efficiency is given by binomial statistics as

$$\Delta\varepsilon = \sqrt{\frac{\varepsilon(1-\varepsilon)}{N_{\text{tot}}}}, \tag{1}$$

where N_{tot} is the total number of signals injected on the shell. We then plot the average detection efficiency as a function of the shell radius and fit a sigmoid to the data; to quantify the detection efficiency of that search, we use this fit to interpolate the distance at which the detection efficiency is 50%, herein referred to as *reach* and denoted
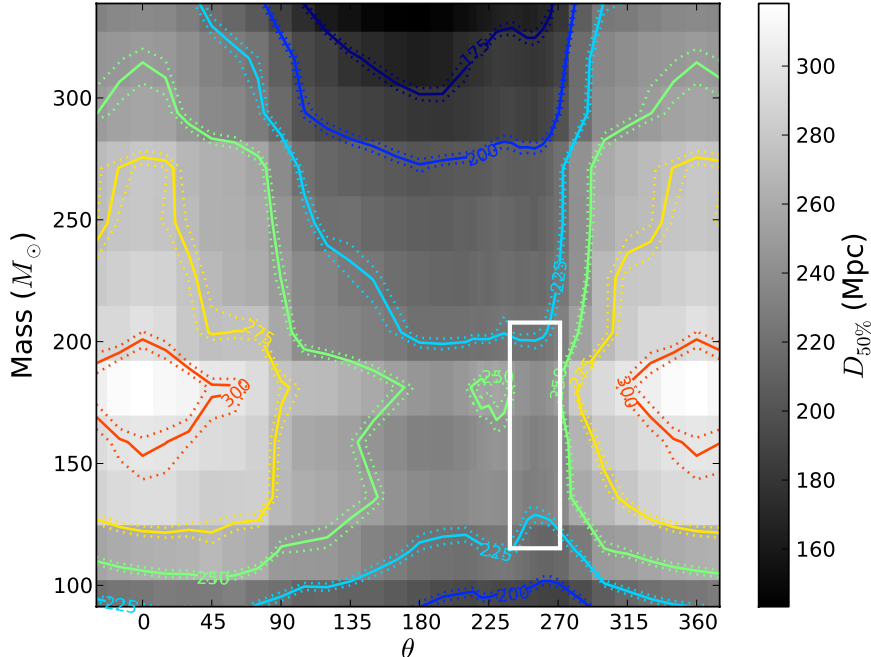
FIG. 6: Reach for the system discussed in Section IV, where the adimensional spin of each black hole is 0.6, using only the $(\ell, m) = (2, \pm 2)$ modes of the waveforms. To clarify features at the left and right edges of the plot, four angles were repeated. Dotted lines in the contours represent uncertainties from the limited statistics of the runs. Notice that the trend appears to go roughly as the total angular momentum of the system: when $\theta = 0°$, one of the black holes is spin "up", parallel to the orbital angular momentum; when $\theta = 180°$, it is spin "down", antiparallel to the orbital angular momentum. This trend is broken by an asymmetry near $\theta = 255°$ for masses between 125 and 300 $M_\odot$; the white rectangle marks the location where this is most pronounced.

by $D_{50\%}$. The uncertainty in the reach is propagated from the uncertainty in the sigmoid fit parameters, which are calculated by the ROOT MINUIT [48] toolkit from the uncertainties $\Delta\varepsilon$ in the individual detection efficiency data points; the resulting reach uncertainties are drawn as error bars in the figures of reach versus simulation parameters. In Figure 5, we show the fit for the case of $a/m = 0.6$, $\theta = 0°$, $d/M = 6.2$. Error bars are drawn on each point, equal to $\Delta\varepsilon$, although they are too small to be visible at this scale.

IV. RESULTS

This study focuses on the dependence of detection efficiency on the orientation and magnitude of the spins of the two merging black holes.

The system under study consists of two equal-mass black holes with the same spin magnitude. In the coordinate system where the initial orbital angular momentum of the system is in the $+z$ direction, the initial spin of one black hole is in the $-x$ direction, while the initial spin of the second black hole is oriented at an angle θ from the $+z$ direction, as sketched in Figure 1. We examine the dependence of detection efficiency on both the magnitude of the spins and the parameter θ.

A. Dependence on total mass

We begin with a system where the magnitude of the adimensional spin of each black hole is 0.6. Numerical simulations were generated for θ ranging from 0° to 345°, and the mass was binned into twelve bins, 22.5 $M_\odot$ wide, to produce a contour plot of the reach in the $M - \theta$ plane as shown in Figure 6. For a given value of θ, the reach peaks at $\approx 180\ M_\odot$. This reflects how the waveform frequency structure scales with the system total mass: at $\approx 180\ M_\odot$,
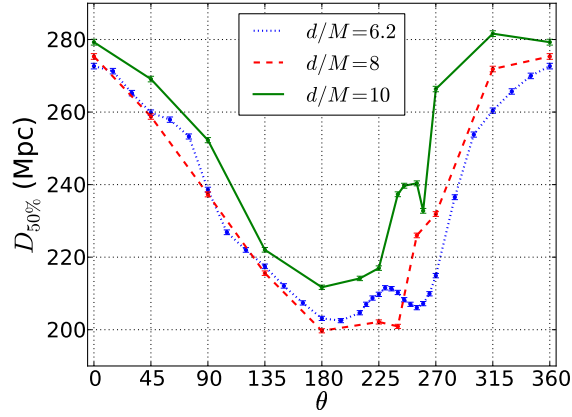
FIG. 7: Average reach in $80 - 350\ M_\odot$ as a function of θ for systems with different initial black hole coordinate separations. The dotted line is $d/M = 6.2$, dashed is $d/M = 8$, and solid is $d/M = 10$.

the merger falls into the detector's most sensitive frequency band. As the total mass of the system either increases or decreases, the waveform portion triggering Omega correspondingly moves later or earlier into the waveform, where less power is emitted, and consequently the reach is reduced [30, 49]. This feature is well understood, and not unique to this particular system.

B. Dependence on spin orientation

Figure 6 shows that, at a given mass, the reach peaks at $\theta = 0°$ and has a minimum near $\theta = 180°$, though its precise location depends on the total mass. Keeping in mind that at $\theta = 0°$ one of the black holes is spin "up", parallel to the orbital angular momentum, and at $\theta = 180°$ it is spin "down", antiparallel to the orbital angular momentum, the reach appears to go roughly as the radiated energy and angular momentum of the system. The reach deviates from the total energy radiated in the vicinity of $\theta = 255°$ and is instead more evocative of J_z^{rad} and of the dominant $(\ell, m) = (2, \pm 2)$ modes contribution to E^{rad}, as seen in Figures 2 and 3, respectively.
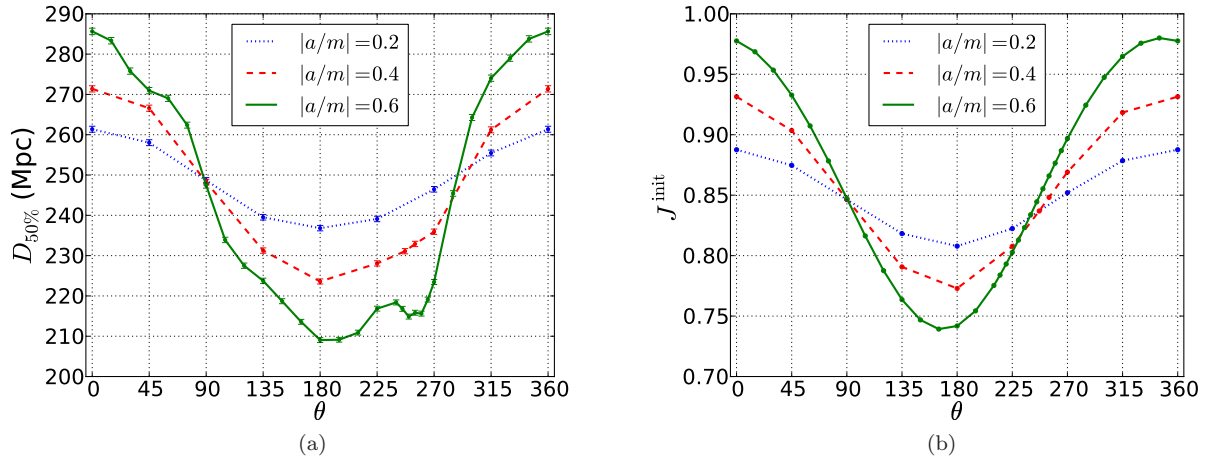

FIG. 8: Panel (a): reach as a function of θ for the system sketched in Figure 1 with $a/m = 0.2$, 0.4, and 0.6, averaged over $80 - 350\ M_\odot$: $a/m = 0.2$ is the dotted line, $a/m = 0.4$ the dashed, $a/m = 0.6$ the solid. The three systems exhibit a similar behavior, proportional to the spin magnitude. Panel (b): the initial angular momentum is plotted versus θ for the same three spin magnitudes.
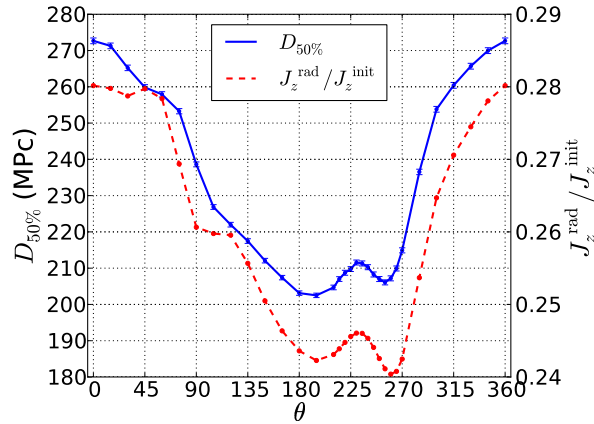
FIG. 9: Average reach in the $80 - 350$ $M_\odot$ mass range, as a function of θ, compared to the normalized z-component of the radiated angular momentum. Only the dominant $m = \pm 2$ modes are included.

C. Dependence on initial coordinate separation

Since the waveforms used to generate Figure 6 were relatively short, with only a few cycles before merger, we repeated the analysis with waveforms of different lengths and compared simulations with initial coordinate separations d/M of 6.2, 8, and 10; the system in Figure 6 has $d/M = 6.2$. The results, averaged over the entire mass range, are shown in Figure 7. The individual spins of the black holes, as well as the orbital angular momentum, will in general precess about the total angular momentum of the system. Therefore, two simulations of different lengths with the same initial value of θ will in general *not* represent the same system. We are interested, however, not in confirming point-by-point agreement between the simulations, but rather agreement in the overall behavior of the reach for the different simulations lengths. All three simulation sets exhibit the same sinusoidal behavior observed in the shorter simulations and, to varying degree, the asymmetry at $\theta = 255°$. The effect is more subtle in the simulations with $d/M = 8$ due to sparse θ sampling in the region surrounding the $\theta = 255°$.
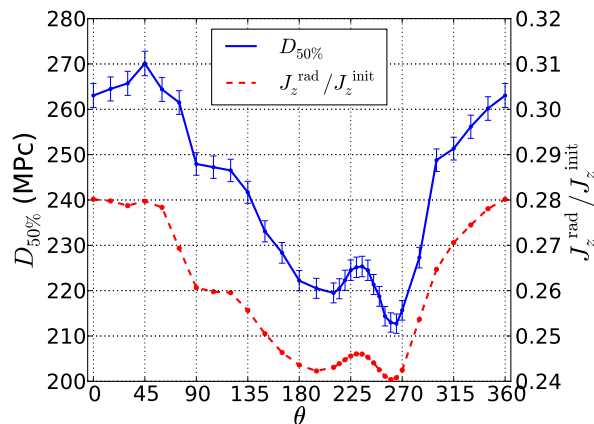

FIG. 10: Reach as a function of θ, restricted to $102.5 - 125.0$ $M_\odot$, compared to the normalized z-component of the radiated angular momentum. Only the dominant $m = \pm 2$ modes are included.

D. Dependence on spin magnitude

Next, we compare the behavior of the same system for adimensional spin magnitudes 0.2, 0.4, and 0.6. For a comparative analysis, we forgo breaking up the data into mass bins, and instead show the average reach in the
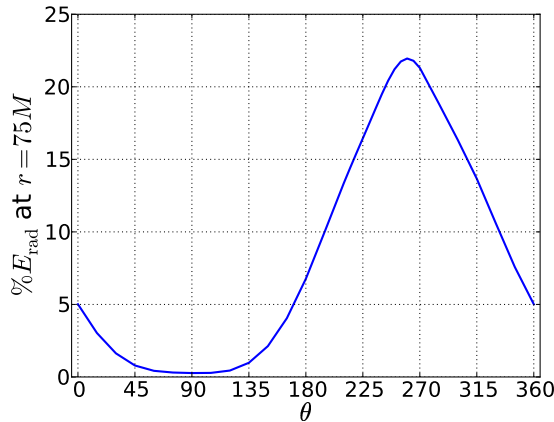
FIG. 11: Percentage of energy radiated by the non-dominant modes as a function of θ.

$80 - 350$ $M_\odot$ mass range in Figure 8(a). All three systems exhibit the same bulk behavior, with a peak at $\theta = 0°$ and a minimum at $\theta = 180°$. The asymmetry in θ is evident for spin 0.6, but it does not show in the lower spin cases in Figure 8(a), due to the combination of two factors: for practical reasons, θ was sampled less at spin 0.4 and 0.2 than at spin 0.6, and the amount of angular momentum radiated in the x direction decreases with decreasing spin, as the precession is decreasing. Overall, we find that the variation of the reach is proportional to the magnitude of the black hole spins, which is consistent with the observation that the reach scales with the total angular momentum of the system. For comparison, Figure 8(b) shows how the initial angular momentum of the system depends on the spin magnitude, as a function of the angle θ.

E. Correlation with radiated energy and angular momentum

The asymmetry of the reach versus θ, seen near $\theta = 255°$ is over-emphasized, since our original analysis did not include all the $\ell = 2$ modes. Figures 9 and 10 show the reach calculated with only the $\ell = |m| = 2$ modes versus θ for two choices of total mass for the system with $a/m = 0.6$ and $d/M = 6.2$. In Figure 9, the reach is averaged over the entire mass range of $80 - 350M_\odot$ while in Figure 10 one bin of total mass is selected: $102.5 - 125.0M_\odot$. In each of these plots, $J_z^{\rm rad}/J_z^{\rm init}$ is included for reference.

Comparing the reach calculated from just the $\ell = |m| = 2$ modes with that calculated from all the $\ell = 2$ modes in Figures 12 and 13, it is clear that the reach asymmetry is alleviated with the inclusion of all the $\ell = 2$ modes.

The dependence of the reach on z-component $J_z^{\rm rad}$, rather than the total radiated angular momentum $J^{\rm rad}$, when only the $\ell = 2$, $m = \pm 2$ modes were used in the calculations, is explained by Equations (3.22)-(3.24) from [50], where the radiated momentum in the x and y directions depends on non-zero $m \neq \ell$ harmonics. Likewise, we get the same effect if one ignores the $m \neq \ell$ modes in calculating the radiated energy. Figure 11 gives a clear indication of why the value $\theta = 255°$ appears "special" in our choice of initial data by plotting the percent energy radiated in the non-dominant $\ell = 2$ modes.

The reach calculated with all the $\ell = 2$ modes and averaged over the $80 - 350M_\odot$ mass range, shown in Figure 13, is well represented by the radiated energy. The reach, however, does depend on the mass range, as seen for instance in Figure 14. In particular, the lower mass bins of data are well described by the radiated angular momentum rather than the radiated energy. We speculate that at low masses, the Omega algorithm tends to trigger earlier in the waveform, when most of the angular momentum is being radiated. On the other hand, when averaged over the full mass-scale, the reach takes on the characteristic of radiated energy, shown in Figure 2 as we would have expected.

V. CONCLUSIONS

We used simulated waveforms for BBH coalescences, calculated with the MAYAKRANC code, to characterize the detection efficiency of the LIGO-Virgo Omega burst algorithm as a function of the morphological parameters of the system and to investigate the algorithm's response to bulk features in gravitational waves from BBH mergers. We chose one particular set of equal-mass, quasi-circular, spinning waveforms that allow for precession; for fixed initial
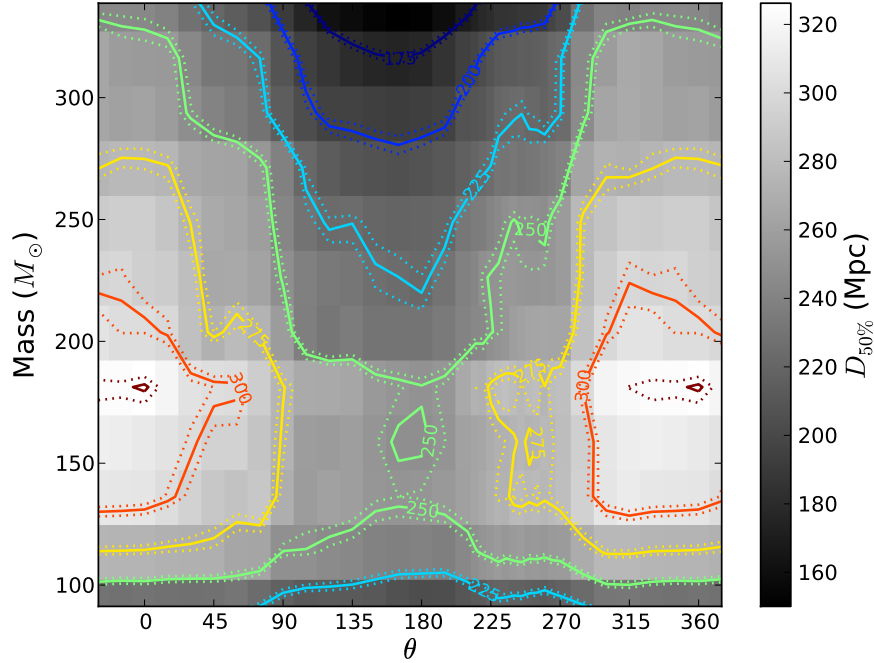
FIG. 12: Same as Figure 6, but using all $\ell = 2$ modes of the waveforms. Notice that the asymmetry at $\theta = 255°$ is significantly reduced by the addition of the additional modes.
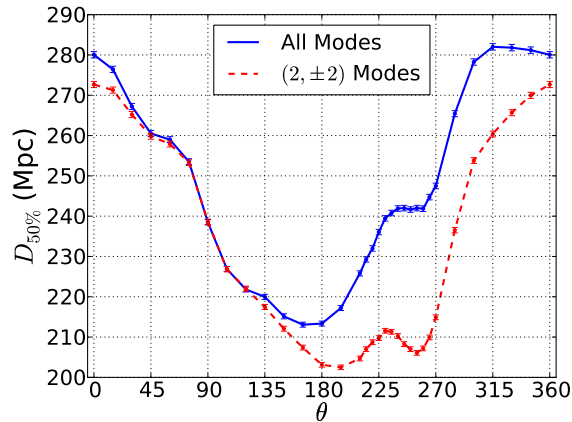

FIG. 13: Reach as a function of θ averaged over the entire mass range $80 - 350 \, M_\odot$ for injected signals using only the dominant $(\ell, m) = (2, \pm 2)$ modes and injected signals using all $\ell = 2$ modes. Notice that in the vicinity of $\theta = 90°$, the curves agree very well, because this is where the black hole spins are antiparallel and cancel, making the contributions of the $m = 0$ and $m = \pm 1$ modes negligible. As θ moves away from 90, the additional modes become more important, and the curves differ very significantly.

spin magnitudes and fixed initial separation of the black holes in the simulations, we investigated the dependence of the detection efficiency on the orientation of the initial spin vector of one of the black holes, parametrized by the angle θ between such spin and the angular momentum of the system.

As θ is varied, the initial angular momentum changes as in Figure 8(b), resulting in different dynamics of the binary. The detection reach, established with the Omega burst algorithm, is sensitive to such differences, peaking when the initial black-hole spin vector is $\theta = 0°$ and dipping near $180°$, consistent with the system's initial angular momentum. A departure from this trend, noted near $\theta = 255°$, is an indication that non-dominant modes are important in these
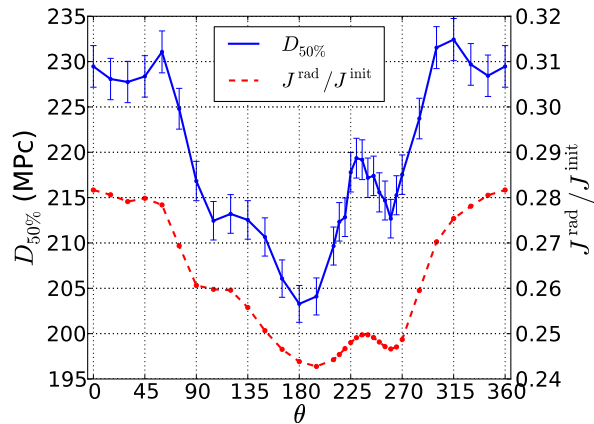
FIG. 14: The solid curve is the reach computed using all $\ell = 2$ modes, constricted to the lowest mass range $80 - 102.5 \ M_{\odot}$. This is compared to the radiated angular momentum J^{rad} normalized to the initial angular momentum J^{init}, the red dashed curve. Note that the two curves appear to have very similar behavior, indicating that the detection efficiency of simulated signals including all $\ell = 2$ modes is roughly proportional to the radiated angular momentum.

systems. If all the $\ell = 2$ modes are included in the simulations, the reach is well understood by the radiated energy when averaging over the entire mass range studied, $80 - 350 M_{\odot}$; however, when the reach is computed at the low-end of the mass range its behavior is more evocative of radiated angular momentum. We conclude that it is important to account for all $m \neq \ell$ modes to both compute the full radiated angular momentum and to measure the detection reach of a burst search for precessing BBH systems.

For non-precessing, aligned-spin, equal-mass systems, the higher the magnitude of the black-hole spins, the greater the reach, since the system radiates more angular momentum [51]. For precessing systems, we find the reach depends on the orientation of the spins: higher-spin systems have a greater reach when the J_z^{init} is at a maximum and the spin is aligned with the orbital angular momentum, near $\theta = 0°$, but a lower reach when J_z^{init} is at a minimum, when the spin anti-aligned, near $\theta = 180°$. We find the variation of reach with θ is proportional to the magnitude of the black hole spins. For a system with two equal magnitude spins of 0.6, the reach variation with orientation is $\sim 30\%$, resulting in a $\sim 120\%$ difference in sensitive volume and in the rate of detectable precessing BBH in initial and advanced interferometric detectors.

The parameter space of BBHs is large and this work targets only a portion of it. In future studies, we will continue to explore the search algorithm's response to the parameters of precessing systems, such as the black hole mass ratio, and investigate how degeneracies in the detectable parameter space caused by the transition from a largely parametrized inspiral phase to a two-parameter end state impacts burst algorithms' ability to extract the system's physical properties.

Acknowledgments

[1] B. Abbott et al., Rep. Prog. Phys. **72**, 076901 (2009).
[2] F. Acernese et al., Class. Quant. Grav. **23**, S635 (2006).
[3] J. R. Smith et al., Class. Quant. Grav. **26**, 114013 (2009).
[4] Virgo Collaboration, <u>Advanced Virgo Baseline Design</u>, note VIR-027A-09 May 16, 2009.
[5] J. Abadie et al., Class. Quant. Grav. **27**, 173001 (2010).
[6] J. Abadie et al., Phys. Rev. **D81**, 102001 (2010).
[7] B. P. Abbott et al., Phys. Rev. **D80**, 102001 (2009).
[8] F. Pretorius, Phys. Rev. Lett. **95**, 121101 (2005).
[9] M. Campanelli, C. O. Lousto, P. Marronetti, and Y. Zlochower, Phys. Rev. Lett. **96**, 111101 (2006).
[10] J. G. Baker, J. Centrella, D.-I. Choi, M. Koppitz, and J. van Meter, Phys. Rev. Lett. **96**, 111102 (2006).
[11] F. Herrmann, I. Hinder, D. Shoemaker, and P. Laguna, Class. Quant. Grav. (2007).
[12] J. G. Baker et al., Astrophys. J. **653**, L93 (2006).
[13] J. A. Gonzalez, U. Sperhake, B. Brügmann, M. Hannam, and S. Husa, Phys. Rev. Lett. **98**, 091101 (2007).
[14] F. Herrmann, I. Hinder, D. Shoemaker, P. Laguna, and R. A. Matzner, Astrophys. J. **661**, 430 (2007).
[15] M. Koppitz et al., Phys. Rev. Lett. **99**, 041102 (2007).
[16] M. Campanelli, C. O. Lousto, Y. Zlochower, and D. Merritt, Astrophys. J. **659**, L5 (2007).
[17] J. A. Gonzalez, M. D. Hannam, U. Sperhake, B. Brügmann, and S. Husa, Phys. Rev. Lett. **98**, 231101 (2007).
[18] W. Tichy and P. Marronetti, Phys. Rev. D **76**, 061502 (2007).
[19] M. Campanelli, C. O. Lousto, Y. Zlochower, and D. Merritt, Phys. Rev. Lett. **98**, 231102 (2007).
[20] J. G. Baker et al., Astrophys. J. **668**, 1140 (2007).
[21] F. Herrmann, I. Hinder, D. M. Shoemaker, P. Laguna, and R. A. Matzner, Phys. Rev. D **76**, 084032 (2007).
[22] B. Brügmann, J. A. Gonzalez, M. Hannam, S. Husa, and U. Sperhake, Phys. Rev. D **77**, 124047 (2008).
[23] J. D. Schnittman et al., Phys. Rev. D **77**, 044031 (2008).
[24] D. Pollney et al., Phys. Rev. D **76**, 124002 (2007).
[25] C. O. Lousto and Y. Zlochower, Phys. Rev. D **77**, 044028 (2008).
[26] J. G. Baker et al., Astrophys. J. **682**, L29 (2008).
[27] S. Dain, C. O. Lousto, and Y. Zlochower, Phys. Rev. D **78**, 024039 (2008).
[28] J. Healy, F. Herrmann, I. Hinder, D. M. Shoemaker, P. Laguna, and R. A. Matzner, Phys. Rev. Lett. **102**, 041101 (2009).
[29] J. A. Gonzalez, U. Sperhake, and B. Brügmann, Phys. Rev. D **79**, 124006 (2009).
[30] B. Aylott et al., Class. Quant. Grav. **26**, 165008 (2009).
[31] A. Buonanno et al., Phys. Rev. D **76**, 104049 (2007).
[32] P. Ajith et al. (2009), arXiv:0909.2867 [gr-qc].
[33] R. Sturani et al. (2010), 1005.0551.
[34] <u>The Omega Pipeline</u>, URL `https://geco.phys.columbia.edu/omega`.
[35] B. P. Abbott et al. (LIGO Scientific), Phys. Rev. D **80**, 047101 (2009), 0905.3710.
[36] J. Healy, J. Levin, and D. Shoemaker, Phys. Rev. Lett. **103**, 131101 (2009).
[37] J. Healy, P. Laguna, R. A. Matzner, and D. M. Shoemaker, Phys. Rev. **D81**, 081501 (2010).
[38] I. Hinder, B. Vaishnav, F. Herrmann, D. Shoemaker, and P. Laguna, Phys. Rev. D **77**, 081502 (2008).
[39] S. Husa, I. Hinder, and C. Lechner, Computer Physics Communications **174**, 983 (2006).
[40] J. M. Bowen and J. York, James W., Phys. Rev. D **21**, 2047 (1980).
[41] M. Ansorg, B. Brügmann, and W. Tichy, Phys. Rev. D **70**, 064011 (2004).
[42] L. E. Kidder, Phys. Rev. D **52**, 821 (1995).
[43] T. Damour, P. Jaranowski, and G. Schaefer, Phys. Rev. **D62**, 044024 (2000).
[44] E. Schnetter, S. H. Hawley, and I. Hawke, Class. Quant. Grav. **21**, 1465 (2004).
[45] cactus-web, cactus Computational Toolkit home page: `http://www.cactuscode.org`.
[46] D. A. Brown et al. (2007), 0709.0093.
[47] C. Reisswig and D. Pollney (2010), 1006.1632.
[48] F. James, <u>MINUIT - Function Minimization and Error Analysis - Reference Manual</u> (2000), URL `http://wwwasdoc.web.cern.ch/wwwasdoc/minuit/minmain.html`.
[49] L. Cadonati et al., Class. Quant. Grav. **26**, 204005 (2009).
[50] M. Ruiz, M. Alcubierre, D. Núñez, and R. Takahashi, General Relativity and Gravitation **40**, 1705 (2008).
[51] C. Reisswig et al., Phys. Rev. D **80**, 124026 (2009).